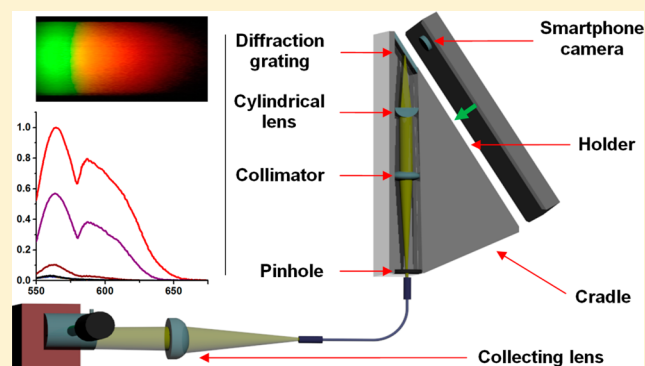


Smartphone Fluorescence Spectroscopy

Hojeong Yu,[†] Yafang Tan,[†] and Brian T. Cunningham^{*,†,‡}[†]Department of Electrical and Computer Engineering, Micro and Nanotechnology Laboratory, University of Illinois at Urbana–Champaign, 208 North Wright Street, Urbana, Illinois 61801, United States[‡]Department of Bioengineering, Micro and Nanotechnology Laboratory, University of Illinois at Urbana–Champaign, 208 North Wright Street, Urbana, Illinois 61801, United States

S Supporting Information

ABSTRACT: We demonstrate the first use of smartphone spectrophotometry for readout of fluorescence-based biological assays. We evaluated the smartphone fluorimeter in the context of a fluorescent molecular beacon (MB) assay for detection of specific nucleic acid sequences in a liquid test sample and compared performance against a conventional laboratory fluorimeter. The capability of distinguishing a one-point mismatch is also demonstrated by detecting single-base mutation in target nucleic acids. Our approach offers a route toward portable biomolecular assays for viral/bacterial pathogens, disease biomarkers, and toxins.



There is tremendous interest in transition laboratory-based biomolecular assays to mobile platforms that would enable disease diagnostics tests, pathogen detection, and toxin detection to be performed in point-of-use scenarios. Since the introduction of smartphones, hundreds of millions of the devices have been sold, with competition among platforms resulting in ever-increasing capabilities for computation, display, and sensing. In particular, smartphone cameras developed for producing high pixel-count images and operating under low-light conditions have proven sufficient for fluorescence microscopy capable of observing individual fluorescent nanoparticles,¹ detection of the output of photonic crystal biosensors,² and colorimetric spectroscopy of colored liquids in enzyme linked immunosorbent assays (ELISA).³ In each of these cases, the smartphone camera was used as a sensor to perform functions equivalent to much larger and more expensive laboratory instruments.

Light-emitting reporters are the most commonly used tools for studying the interactions between biomolecules and for imaging cell structures in applications that include genomics,^{4–8} proteomics,^{9–12} disease diagnostics,^{13–15} life science research,¹⁶ and drug discovery.^{17–20} Light emitters operate via a variety of optical mechanisms that include fluorescence,^{21–23} chemoluminescence,^{24,25} phosphorescence,²⁶ and semiconductor quantum dot^{27–30} excited electron relaxation. Photon-emitting biomolecular tags have taken a dominant role due to ease of coupling covalently to most biomolecules, the wide variety of inexpensive/compact excitation sources, and the range of available excitation/emission wavelengths. Among these approaches, those that utilize the Förster resonance energy transfer (FRET) as a mechanism for observing changes in the quenching efficiency between matched donor–acceptor pairs

are effective methods for diagnostics applications because single-step assays are performed in liquid, without complex mixing-washing steps, by adding the test sample to a solution that contains a fluorophore-tagged probe molecule that specifically recognizes its intended target. For FRET assays, the ability to measure the spectrum of fluorescent emission is especially useful, as the combined contributions of donor and acceptor fluorophores can be measured independently, while wavelength-selective filters are not necessary. The importance of using mobile platforms, for FRET-based fluorescent assays, has been previously recognized using quantum dots that are carefully selected to emit specifically within the red–green–blue (RGB) passbands of the internal color filters of camera pixels.³¹

In this work, we implement a system that is capable of measuring the full emission spectra of any light emitter (chemical fluorophore or quantum dot) and is thus capable of differentiating a broad range of tags. We demonstrate a simple interface to a conventional smartphone that enables its internal camera to function as a high resolution and sensitive fluorescence spectrometer. By placing a transmission diffraction grating directly in front of the camera (iPhone4 with a 5 megapixel camera (2592 × 1936 pixels)), along with optics for collimating light emitted from a liquid fluorescent sample onto the grating, an emission spectrum is distributed across the pixels of a complementary metal-oxide semiconductor (CMOS) image sensor with a single-pixel wavelength incre-

Received: June 5, 2014

Accepted: August 6, 2014

Published: August 6, 2014

ment of 0.338 nm/pixel. We demonstrate that the smartphone fluorimeter is capable of performing a sensitive molecular-beacon FRET assay for a specific microRNA sequence with performance that is better than a conventional laboratory fluorimeter, with a detection limit, the lowest measured concentration that has an intensity value greater than three standard deviations above the negative control value, of 10 pM. Our results show that smartphone-based spectroscopic fluorimetry is a route toward portable biomolecular assays for viral/bacterial pathogens, disease biomarkers, and toxins, and this general-purpose approach may be extended to other photon-producing assay platforms such as FP, chemoluminescence, and fluorescent-tagged sandwich assays. The resulting capability may find applications that include point-of-care detection/analysis of pathogens, specific nanoparticle detection, human/animal diagnostics, and food safety.

MATERIALS AND METHODS

Smartphone Fluorimeter System. A schematic of the optical system is shown in Figure 1. A custom-designed cradle (Figure S1, Supporting Information) interfaces the rear-facing camera of the smartphone (iPhone4; Apple Inc., CA, USA) with the optical components required to gather, collimate, and disperse light from a small volume of liquid that contains fluorescent emitters. The cradle mechanically aligns a diffraction grating (GT13-12; Thorlabs Inc., NJ, USA), a cylindrical lens (NT48-354; Edmund Optics Inc., NJ, USA), a collimating lens (NT63-491; Edmund Optics Inc.), and a pinhole (NT56-291; Edmund Optics Inc.). In this work, a transparent sample cuvette (16.100F-Q-10/Z15; Globe Scientific Inc., NJ, USA), a laser excitation source (a green laser pointer; Sunplora, Guangdong, China), a focusing lens (LJ1402L1; Thorlabs Inc.), a collecting lens (LA1131; Thorlabs Inc.), and an optical fiber (P1000-2-UV-VIS; Ocean Optics, FL, USA) are external to the cradle body. While holding all components in correct alignment, the cradle prevents external light sources from reaching the camera. In order to minimize the collection of light from the excitation laser into the optical fiber, the sample is illuminated at an orthogonal angle to the light collection axis. A cylindrical lens (focal length (f_1) = 40 mm) is set in front of a green laser pointer (power = 300 mW, wavelength = 532 nm) to create a focused line, centered inside the cuvette. The focal point of the collection lens (focal length (f_2) = 50 mm) is at the same center point of the cuvette. The opposing focal point of the collection lens is located at the end face of an optical fiber (core diameter = 1 mm), as shown in Figure 1a. Light emerging from the distal end of the fiber is a quasi-collimated point source that is further collimated by the pinhole (aperture diameter = 1 mm) and collimating lens (focal length (f_3) = 75 mm) before incidence upon the cylindrical lens (focal length (f_4) = 50 mm) which focuses incident light along only one axis onto the transmission diffraction grating (1200 lines/mm), oriented at a 47 degree angle with respect to the light path in order to match the grating first-order diffraction mode. Finally, the grating disperses the light onto the smartphone CMOS image sensor, enabling separation of the spectral components that can be observed in a photo as a multicolored band as shown in Figure 1b. The internal camera is sensitive to wavelengths within the visible spectrum, $400 < \lambda < 700$ nm. The width of the colored band in the image is ~ 180 pixels (in the nonspectral direction), enabling the spectral intensity of each wavelength to be integrated from the contribution of many independent sensors. Considering the

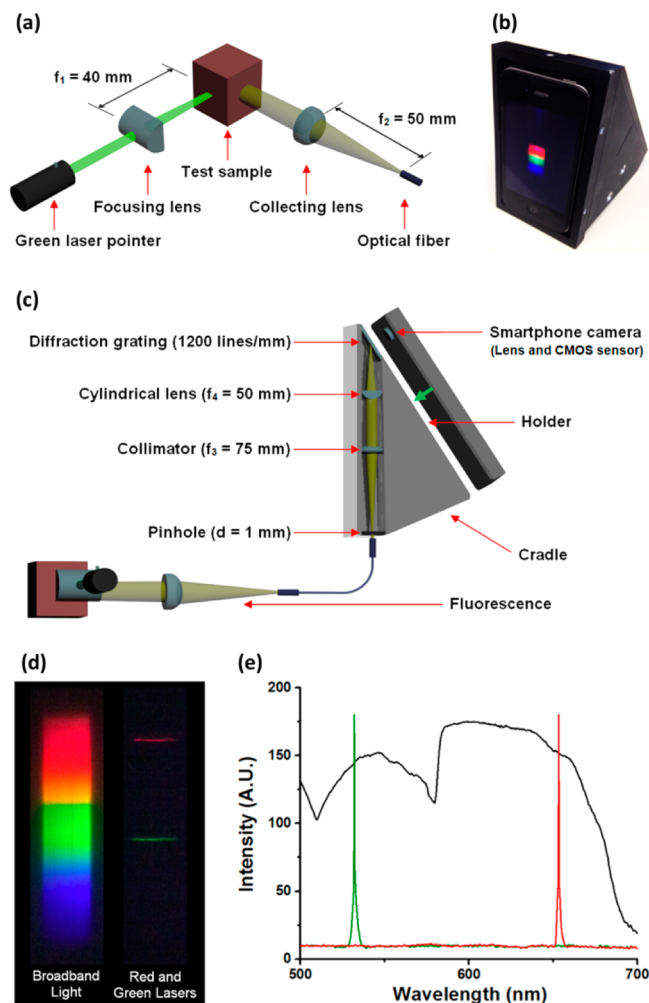


Figure 1. Illustration of the smartphone fluorimeter system and its broadband light source/two laser sources responses. (a, c) Scheme of the smartphone-based fluorescence detection platform. The focus enhanced excitation laser (532 nm) illuminates a cuvette containing the probe-target duplexes. Fluorophores linked to one end of the molecular beacon probes are excited to emit fluorescence in all directions. A portion of the emission is gathered by a collecting lens oriented perpendicular to the laser and enters the cradle, where it is further collimated before incidence upon a diffraction grating placed directly in front of the camera. (b) Photo of the optical cradle installed on the smartphone. The screen of the smartphone shows a spectrum of the transmitted light dispersed by the grating. (d) Images of broadband light, red and green laser beams over smartphone screen. (e) Light intensity distributions of two lasers (green laser: solid green line with $\lambda_{\text{green}} = 532$ nm, red laser: solid red line with $\lambda_{\text{red}} = 653.26$ nm) and a broadband light source (solid black line) measured by the smartphone fluorimeter. Corresponding wavelengths are determined by pixel-wavelength calibration with a single-pixel wavelength increment of 0.338 nm/pixel.

camera pixel resolution and the wavelength range, the smartphone-based fluorimeter has a dispersion of 0.338 nm/pixel in the spectral direction. The fluorescence from the target molecule is analyzed at the ensemble level using target solutions at various concentrations in a standard 2-window polystyrene cuvette.

Preparation of Molecular Beacon Probes. We utilized a molecular beacon (MB) probe and target microRNA-21 (miR-21) pair that has been reported in previous studies.^{32,33} MicroRNAs (miRNAs) are a class of noncoding, single-

Table 1. Characteristics of the Molecular Beacon Probes and the Target miRNAs

molecule	sequence	specification
molecular beacon (MB) probe	5'-GCGCGT CAACA TCAGT CTGAT AAGCT ACGCGC-3' ^a	dye: Cy3 (5' end) quencher: BHQ2 (3' end) total length: 32-nt stem length: 6-nt
mature miR-21	5'-TAGCT TATCA GACTG ATGTT GA-3'	total length: 22-nt perfectly complementary to the loop region of a MB probe
target miRNAs		
mutant mature miR-21	5'-TA <u>ACT</u> TATCA GACTG ATGTT GA-3' ^b	total length: 22-nt single-base mutation ("G" to "A")

^aBases complementary to the mature miR-21 target sequences are underlined in boldface. ^bThe mutated single-base is underlined in italic.

stranded, endogenous ~22-nt RNAs that can play important regulatory roles in animals and plants by targeting miRNAs for degradation or translational repression. They are regarded as key components in gene regulatory pathways and occur in three different forms: long pri-miRNAs, hairpin pre-miRNAs, and short mature miRNAs. Only the mature miRNAs trigger post-transcriptional regulation of the target miRNAs (T-miRNAs) mediated by a specific set of effector proteins and, in human tissues, over 1400 miRNAs have been identified.³⁴ The miR-21 target represents one of the first mammalian miRNAs identified and has been associated with cardiovascular disease,^{35–41} through its role in cardiac cell growth, apoptosis, vascular smooth muscle cell proliferation, and cardiac fibroblast function. The target sequence has also been found to be consistently upregulated in several cancerous tissues. Thus, it has been studied as a potential disease biomarker,^{42,43} and an efficient and simple assessment method of miR-21 would be useful for diagnostics and identifying therapeutic targets.

As described previously,^{22,32,33,44–47} molecule beacons are functional engineered nucleic acid molecules that can selectively interact with a target DNA or RNA sequence in a test sample to render an observable positive change in photon output when the molecular beacon binds with its complementary target. Briefly, molecular beacons are single-strand nucleic acid probes composed of three different functional domains: a loop, a stem, and a fluorophore/quencher pair. When the donor fluorophore absorbs a photon within its range of excitation wavelengths, it is excited to a high energy state that can relax back to the ground state via emission of a photon with a characteristic emission spectrum. When the donor fluorophore is in close proximity to a secondary molecule (quencher) with an absorption spectrum that overlaps the donor emission spectrum, the donor emission energy is transferred in a nonradiative fashion through long-range dipole–dipole coupling via FRET. When the acceptor quencher is coupled to the donor fluorophore, little or no fluorescence emission from the donor can be measured. However, if the loop region of the molecular beacon encounters and binds with a complementary target nucleic acid sequence, the conformation of the molecular beacon changes. The stem regions of the molecule are forced to open, which consequently separates the donor and acceptor; thus, the fluorophore started to emit specific fluorescence. The 22-nt mature miR-21 (5'-TAGCT TATCA GACTG ATGTT GA-3') is the "target" sequence that we wish to selectively detect, while a 22-nt mutant mature miR-21 (5'-TAACT TATCA GACTG ATGTT GA-3', mismatched base is marked in italic with underline) was used to demonstrate capability of distinguishing single-base mismatch

(Table 1), in which the single-base mutation occurs near the end of the hybridization region. The fluorescence intensity from a probe-target hybrid with mismatched target is related to the target concentration, the number of mismatched bases, and the type of mismatched pair. The molecular beacon solution was diluted to a concentration of 0.5 μ M (75 μ L), while both the mature miR-21 and the mutant mature miR-21 were diluted by phosphate buffered saline (PBS, pH = 7.4) to create seven concentrations of target ranging from 1 pM to 1 μ M (75 μ L each). The detection limit and the concentration dependence of molecular beacon FRET is demonstrated by varying the molar densities of target in the test sample. The 32-nt molecular beacon probes (Cy3-5'-GCGCGT **CAACA TCAGT CTGAT AAGCT** ACGCGC-3'-BHQ2, the complementary region is indicated in bold with underline, stem length = 6-nt) were designed to be complementary to the mature sequence of miR-21. A 32-nt single-strand molecular beacon probe was designed and synthesized containing an internal Cy3 FRET donor (Cyanine 3, maximum excitation wavelength λ_{ex} = 550 nm and maximum emission wavelength λ_{em} = 570 nm) at the 5' end and a BHQ2 FRET acceptor (Black Hole Quencher 2, strong absorption in wavelengths of 550–650 nm) at the 3' end. The loop domain of molecular beacon nucleic acid sequence is intended to hybridize with the mature miR-21. In the absence of target molecule, the residues form a beacon stem that holds the Cy3 donor and the BHQ2 acceptor in close proximity. The mature miR-21, mutant mature miR-21, and molecular beacon probes are hybridized (room temperature, 60 min.) to characterize the presence of targets by emitting fluorescence from Cy3.

FRET efficiency (F.E.) depends on the donor-to-acceptor separation distance r with an inverse sixth power law due to the dipole–dipole coupling process described by the equation:

$$\text{F.E.} = \left[1 + \left(\frac{r}{R_0} \right)^6 \right]^{-1}$$

The Förster distance (R_0) is the distance between two fluorophores when the energy transfer efficiency is 50%. R_0 depends on the mutual molecular orientation of them and the overlap integral of the donor emission spectrum with the acceptor absorption spectrum.^{48,49} R_0 is given by:

$$R_0 = 0.211(n^{-4}\gamma^2J(\lambda)Q_D)^{1/6}$$

where n is the refractive index of the medium, γ^2 is the orientation factor of the interacting dipoles and is generally equal to 2/3, and Q_D is the quantum yield of the donor. $J(\lambda)$ is

the spectral overlap integral between the donor emission and acceptor absorption,

$$J(\lambda) = \int \varepsilon_A(\lambda) f_D(\lambda) \lambda^4 d\lambda$$

where ε_A is the acceptor absorption coefficient and f_D is the peak-normalized donor emission spectrum. The Förster distance between Cy3 and BHQ2 is 5.02 nm. When the hybridization event takes places, the donor and the quencher are spatially separated from each other by ~ 11 nm, resulting in low F.E. (~ 0.009) and most of the energy from the Cy3 donor emitted as fluorescence.

Image Processing. When an ordinary digital photo is taken, the original image is divided into a grid as it is captured by the CMOS sensor. Pixels (the smallest resolvable grid spacing) are normally arranged in a two-dimensional grid, and each pixel of an image is a composite of three subpixels representing the red, green, and blue primary colors. The color information on each pixel is stored in 3 different multilayers of RGB color space. This results in a $2592 \times 1936 \times 3$ matrix whose elements are real numbers ranging from 0 to 255 (8-bit number) for each digital color photo. However, when the camera is operated as a photodetector, we are only concerned with the total intensity gathered by all the subpixels because the hue information is spread over the screen as a color spectrum. Transformation from primary RGB colors to a HSV (Hue-Saturation-Value) color map was performed to provide a photon intensity of each pixel. HSV is a cylindrical coordinate representation of points in a RGB color space, where the V axis represents brightness of a corresponding color determined by $V = \text{Max}(R, G, B)$.⁵⁰ The values from our RGB image were converted into a V image in a $2592 \times 1936 \times 1$ matrix of pixels.

A broadband illumination spectrum from an incandescent lamp (150 W halogen fiber-optic high intensity illuminator; Cole-Parmer, IL, USA) that would ordinarily be smooth and continuous across the visible spectrum results in a smartphone-determined spectrum that includes intensity fall-offs near $\lambda_1 = 510$ nm (cyan) and $\lambda_2 = 580$ nm (yellow). The RGB color filter strongly responds to particular colors (red, green, and blue) to mimic the performance of the human eye, leading to the observed fall-offs between three primary color bands. The broad spectrum from an incandescent lamp is observed as a multicolored band that covers approximately 850 pixels in the dispersion direction and is roughly 180 pixels wide. In order to efficiently use as much of the incident light as possible, an overall intensity value for each spectrum is determined by summing the intensities of all ~ 180 pixels across the colored band's width. The amount of light that reaches the image sensor is proportional to the exposure time of the camera. We used the longest available exposure time, 1 s, limited by the iOS (iPhone Operating System) to maximize fluorescence intensity values.

Wavelength Calibration. A calibrated fiber-optic spectrometer (HR2000; Ocean Optics, FL, USA) and two conventional laser pointers ($\lambda_{\text{red}} = 653.26$ nm, $\lambda_{\text{green}} = 532$ nm, ~ 300 mW) were used to convert each pixel index in the image into its corresponding wavelength value. When the tip of the optical fiber is illuminated with the laser pointers, it results in two sharp bands in the acquired image. Utilizing the known laser wavelengths determined by a reference spectrometer enables assignment of wavelength values to pixel values along the spectral direction of the camera image. We assume a linear relationship between wavelength value and pixel index from the

red and green calibration lasers, resulting in a single-pixel wavelength increment of 0.338 nm/pixel. The calibration is maintained as long as the smartphone remains within the cradle.

As shown in Figure 1e, the optical spectrum measured for an incandescent lamp contains two dips. The dips correspond with regions of the spectrum for which the transmission efficiency of the RGB filters within the smartphone's camera are designed to cut off their respective passbands. Using the scaled difference between the spectrum from a known source of illumination and the spectrum measured with the smartphone spectrometer, it is possible to apply a correction factor that would enable the smartphone to display a spectrum that closely approximates that from any unknown source. In the spectra presented through this paper, no such correction factor has been applied, and the data obtained directly from the smartphone spectrometer without modification are presented.

RESULTS

Fluorescence Detection. The smartphone-based spectroscopic system was used to measure fluorescence emission from a probe-target hybrid with different concentrations of the target molecule, mature miR-21, which has complementary nucleotide sequences to the loop region in the molecular beacon probe (perfect match). Every test sample, including all experimental controls, was also measured with a conventional fluorescence spectrophotometer (Cary Eclipse; Agilent Technologies, CA, USA) that utilizes a Xenon flash lamp ($P_{\text{peak}} \sim 75$ kW) for fluorescence excitation, a photomultiplier tube sensor for detection of emission, and a set of user-selectable excitation/emission filters that enable sensitivity in the 200–900 nm wavelength range.

An initial negative control reading was performed using molecular beacon probes at a concentration of 0.5 μM in PBS without the presence of target analyte. Then, using a series of cuvettes with molecular beacon probes at the same 0.5 μM concentration (one cuvette per target concentration), we prepared perfectly matched mature miR-21 target, over the range of 1 pM to 1 μM concentrations. The molecular beacon probes and miRNA targets were allowed to incubate in the cuvette for 60 min before performing a measurement in the laboratory fluorimeter and the smartphone fluorimeter. Results of the experiment are summarized in Figures 2 and 3.

First, we observe that, without the target mature miR-21 to be hybridized with the molecular beacon probe and to open the stem region, the Cy3 donor fluorophore is efficiently quenched, resulting in a dark image obtained with the smartphone spectrometer (Figure 2a,b). Here, weakly scattered light from the green laser source appears in the spectrum at its expected location. Figure 2c shows that, when the miR-21 is introduced to the MB, the fluorescence emission from probe-target hybrid is easily observed as a colored band at the expected wavelength range (~ 570 nm) on the smartphone screen, confirming the presence of complementary mature miR-21 targets in the test solution.

Figure 3 compares the fluorescence emission spectra from identical samples measured by the smartphone fluorimeter and the laboratory fluorimeter. The fluorescence spectra establishes a baseline “dark” level that can be compared with subsequent measurements using various concentrations of targets in which most of the Cy3 donors will restore their fluorescence by exposure to the complementary target. The fluorescence intensity from probe-target hybrid (1 pM miR-21) is almost

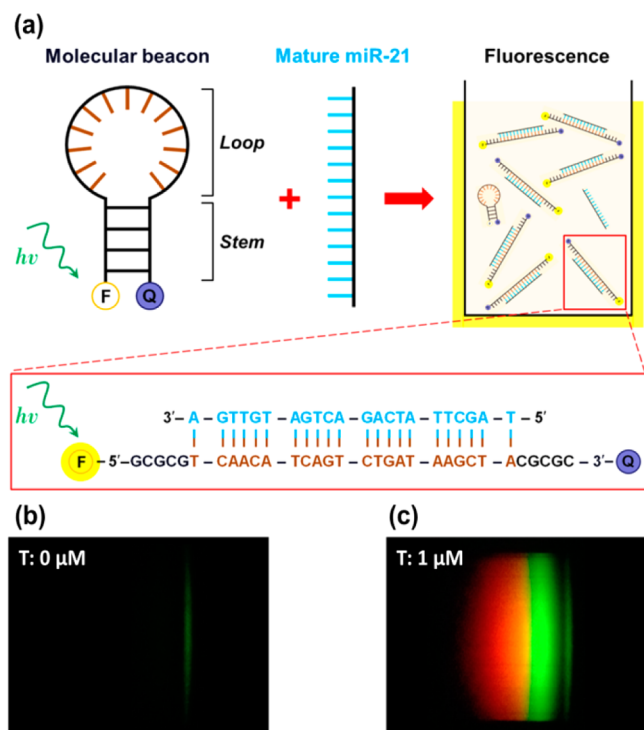


Figure 2. Monitoring probe/target hybridization using molecular beacons technology. (a) Scheme and mechanism of FRET from molecular beacon. Molecular beacons are hairpin-shaped oligonucleotide probes. Each beacon consists of a 5'-Cy3 fluorophore, a 3'-BHQ2 quencher, and an engineered stem-loop sequence. In the presence of a complementary target oligo-nucleotide, the MB probe unfolds to hybridize with the target and then separates the quencher from the fluorophore. Then, the fluorescence from the fluorophore is restored. (b, c) Spectral bands on the smartphone screen, before the target miR-21 is introduced (target miRNA (T): 0 μ M) and after addition of the target that is a complementary match to the probe (T: 1 μ M), which switches on fluorescence resulting in observation of a colored band on the smartphone pixels. Images are rotated through 90° counter-clockwise.

the same as that from a solution containing only molecular beacon probes that is used as negative control. Interestingly, a background fluorescence signal near 570 nm appeared dimly even for the pure MB solution in the smartphone-based measurement because the emission energy from the Cy3 fluorophore is not completely transferred to the BHQ2 quencher. For the same sample, we did not observe significant background near $\lambda = 570$ nm when using the laboratory fluorimeter. The laboratory fluorimeter used for our comparison uses optical transmission filters in combination with a broadband light source to select specific wavelength and delivers light over a much broader band of excitation wavelengths to the sample than a laser. As a result, when the emission wavelength of the fluorophore is not sufficiently displaced from the excitation wavelengths, a tail from the emission spectrum that is not effectively filtered from the photodiode in the laboratory instrument can mask the presence of low intensity fluorescence emission. In contrast, the excitation wavelength of the laser source in the smartphone fluorimeter is far away from the fluorescence emission band and thus cannot contribute to background signals when the emission is detected spectrometrically. As the mature miR-21 concentration is increased from 10 pM to 1 nM, a clearly observable difference in the fluorescence spectrum is measured

from the smartphone fluorimeter, which is similar to that measured with the laboratory fluorimeter. Indeed, as the mature miR-21 concentration is increased, greater difference between the background fluorescence spectrum and the test sample spectrum is measured. The spectrum approaches the expected emission spectrum of Cy3 at a miRNA concentration of 1 μ M. The smartphone instrument imposes its color bias algorithm on the measured spectrum, introducing the “kinks” at $\lambda = 510$ and 580 nm that were also observed for in the spectrum of the incandescent lamp.

In order to convert the spectra into a single fluorescence intensity value (normalized total intensity), we integrated the area between the negative control sample's spectra and the spectra for a given target miR-21 concentration over a wavelength range of 560–580 nm (Cy3 λ_{em} (570 nm) \pm 10 nm). Although the intensity values from the two instruments have a different numerical basis, we may plot and compare the obtained dose–response plot, as shown in Figure 3b,d. Here, each point represents an average value from three independent measurements, and the error bars represent one standard deviation. At concentrations greater than 10 nM, both instruments display dose-dependent changes in the fluorescence intensity. However, for the lowest concentrations, 10 pM to 1 nM, only the output intensity of the smartphone fluorimeter continues to decrease with decreasing target miR-21 concentration. The lowest detectable concentration is defined by the concentration at which the magnitude of the output is greater than three standard deviations above the zero miRNA concentration background (straight blue line in the inset). For the smartphone fluorimeter, the lowest statistically detectable concentration is 10 pM, while the value is 10 nM for the commercial fluorimeter. By extrapolation, we found the limit of detection (LOD) to be 1.3 pM and 3.6 nM respectively.

Detection of Single-Base Mutation. We tested single-base mismatched target (mutant mature miR-21) to demonstrate detection of single-base mismatch. As before, hybridization between a mutant mature miR-21 and a molecular beacon probe is carried out at room temperature for 60 min. In this case, one of the bases in the mature miR-21 was mutated from G to A near the 5' end to yield imperfect base-pairing, which results in lower affinity and stability for probe–target duplex. This leads to reduced fluorescence compared to the fluorescence from the perfectly matched duplex as shown in Figure 4a. The fluorescence intensity from the MB with mismatched target is inversely proportional to the decrease in the concentration of activated MB probe and the number of mismatched bases. For the dose–response characteristic for the assay, fluorescence intensity as a function of target concentration is more gradual than observed for a perfectly matched probe–target duplex.⁵¹ As shown in Figure 4b, when the mutant mature miRNA-21 was not present, fluorescence was not detected. The fluorescence is restored as the hybridization events take place even though the intensity of fluorescence is decreased, compared to the case in which the target sequence is an exact match for the probe. Figure 4c shows the smartphone fluorescence spectrum from a duplex using mismatched target miR-21 with a concentration of 1 μ M. In comparison to the spectrum obtained with a perfectly matched target, there is an obvious difference in fluorescence intensity. Numerical values of fluorescence intensity for exposure of the MB probe to a range of concentrations of the perfectly matched miR-21 and the single-base mismatched miR-21 are shown in Figure 5, in which results from the smartphone fluorimeter and the

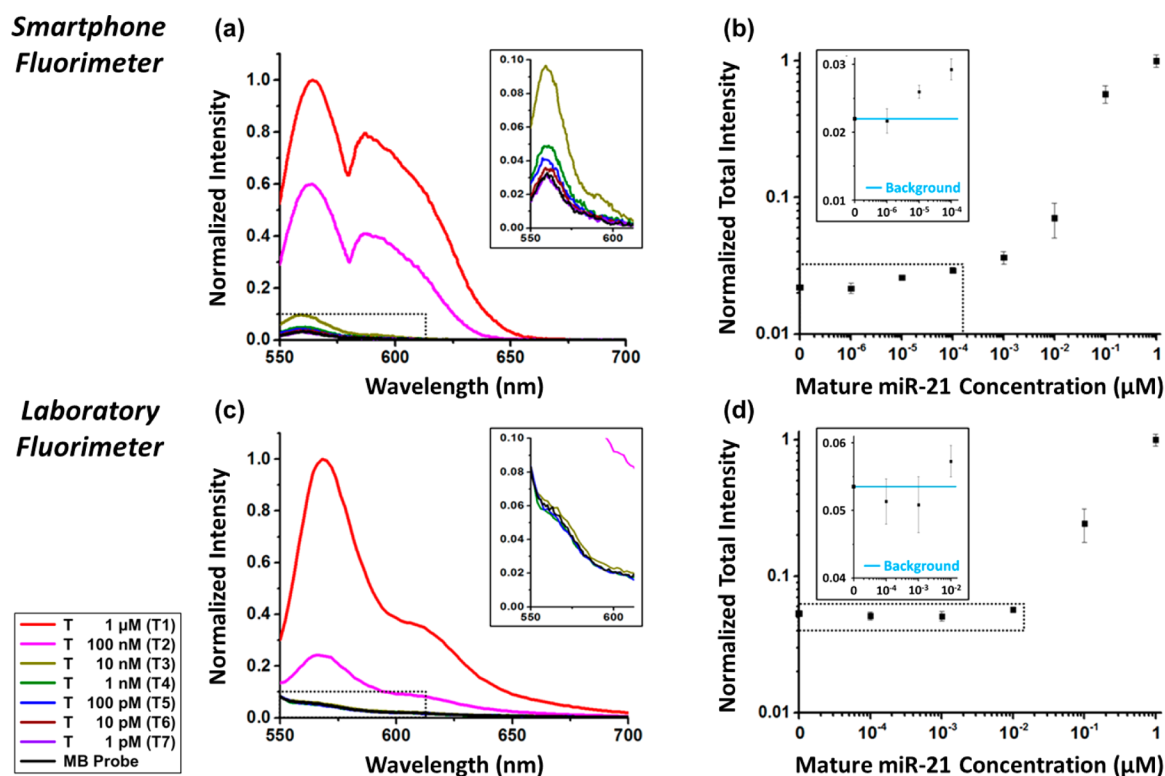


Figure 3. Overall converted fluorescence spectra and plots from the smartphone fluorimeter and the laboratory fluorimeter with different concentrations of T-miRNAs. (a) Normalized fluorescence intensity distributions in the visible spectral domain measured by the smartphone fluorimeter. Inset shows magnified spectra that corresponds to the dashed area. (b) Normalized total intensities according to various T-miRNA concentrations. The intensity over the wavelength range of 560–580 nm was integrated to derive a single intensity value for each concentration. Inset shows enlarged region of the area encompassed by the dashed box. (c, d) Normalized fluorescence intensity distributions and total intensities measured by the laboratory fluorimeter.

laboratory fluorimeter are compared. Significant release of fluorescence from Cy3 donor in MB probes is not observed for both instruments until the mutant miRNA concentration is raised above $0.1 \mu\text{M}$.

DISCUSSION

The experimental demonstrations performed in this work show that the image sensor within a typical smartphone camera is capable of delivering sensitivity performance that is equivalent or superior to that obtained with a conventional laboratory fluorimeter. The differences in sensitivity performance achieved in this study, in which the same assay liquids were measured for both approaches, can be attributed to the differences in the characteristics of the illumination sources and photon sensors.

While the smartphone-based sensing instrument utilizes laser illumination, the Agilent fluorimeter incorporates a Xenon flash lamp. In the smartphone fluorimeter system, the wavelength of excitation source is 532 nm, selected to coincide with 96.7% of the maximum absorption efficiency of Cy3 dye. The output power of the laser source (P_{laser}) is $\sim 300 \text{ mW}$, and the beam diameter is $\sim 1 \text{ mm}$. The number of incident photons from the laser can be predicted by

$$N_{\text{photon}} = \frac{P_{\text{laser}}}{hc/\lambda_{\text{laser}}} \sim 8.03 \times 10^{17} [\text{s}^{-1}]$$

where h is the Planck constant and c is the speed of light. Contrarily, only a small fraction of the output from the Xe lamp falls within the absorption band of Cy3 because the emitted light from the broadband source passes through optical

transmission filters to yield a broader but less intense excitation band. The end output power of the laboratory fluorimeter is $\sim 10 \mu\text{W}$, and the number of incident photons entering the samples is $\sim 2.68 \times 10^{13} [\text{s}^{-1}]$. If we assume that both instruments illuminate equivalent volumes within the cuvette, we estimate that smartphone fluorimeter's laser illumination results in 30 000 \times greater photon delivery compared to the Xe lamp illumination. However, the illumination volumes are not equal in the two approaches. While the Agilent instrument focuses its illumination to a volume of $\sim 1.96 \times 10^{-7} \text{ m}^3$ using a slit, our system utilizes a cylindrical lens to focus light on the cuvette with a volume of $\sim 6.25 \times 10^{-10} \text{ m}^3$. Combining the effects of the illumination method and the illumination volume of analyte, the number of photons in the volume of interest is $\sim 2.65 \times 10^7$ in the smartphone fluorimeter, while the number of photons is $\sim 0.18 \times 10^3$ in the conventional fluorimeter. Thus, we attribute the lower limits of detection obtained with the smartphone fluorimeter, compared with this particular model of a laboratory fluorimeter, to be mainly attributable to differences in illumination geometry and illumination efficiency afforded by selecting a laser as the excitation source.

We may also compare the light collection systems used in the two instruments, which both use dispersion to separate the wavelength components of the emission, in order to generate a spectrum. While the smartphone instrument uses a diffraction grating that spreads the spectrum over the pixels of the CMOS image sensor, enabling all wavelengths of incident light to be measured simultaneously, the laboratory fluorimeter used in our comparison uses a 10 nm wide movable slit, which allows

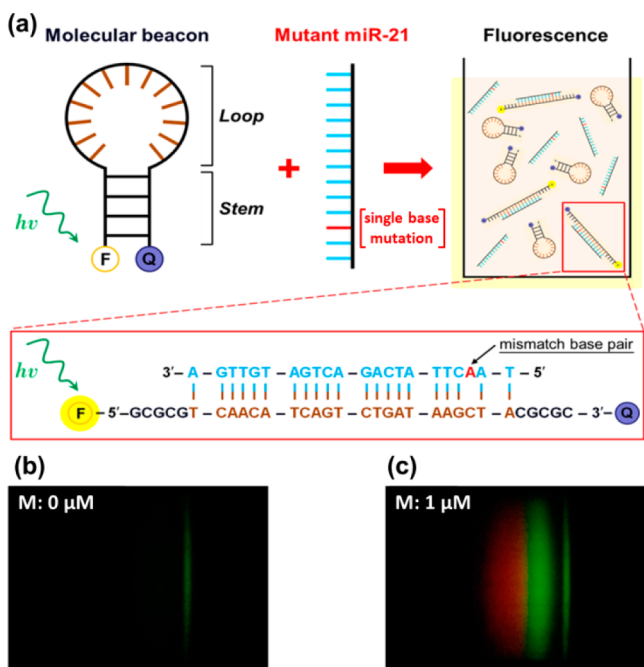
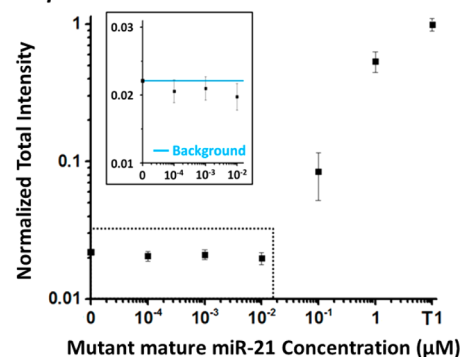


Figure 4. Measuring lighter fluorescence from imperfect probe-target duplex. (a) Scheme of FRET from mismatched target molecule hybridization. One of the bases in mature miR-21 was mutated from G to A. The mutant is indicated in the red-colored “A”. The fluorescence intensity is relatively decreased because a hybridization efficiency is reduced by the single-base mutation (imperfect base-pairing). (b, c) Spectral bands on the smartphone screen. When the mismatched miR-21 is not introduced (mismatched miRNA (M): 0 μ M), only scattered green light was captured like previous measurements using well-matched miRNA. Mismatched probe-target hybrid (M: 1 μ M) provides weaker fluorescence than fluorescence from original probe-target hybrid. Images are rotated 90° counterclockwise.

one wavelength band at a time to illuminate a photomultiplier tube (PMT), where all the photons passing through the slit are integrated to generate the signal from PMT. Specifications for the sensitivity of the iPhone4 CMOS image sensor are not readily available to enable a precise comparison. For the PMT (R928) used in the Agilent fluorimeter, each incident photon on the cathode within the 185–900 nm wavelength range leads to release of an electron by the photoelectric effect, and the electrons arrive at the anode with a gain of 1×10^7 when supply voltage between the cathode and all other electrodes connected together as anode is 100 V. The quantum efficiency of the PMT is $\sim 12\%$ at $\lambda = 570$ nm. These electrons register as a “current” of sensor output. Contrary to this, the conversion gain of a CMOS image sensor is $\sim 40\text{--}160$ $\mu\text{V}/e$ and the quantum efficiency is higher than 40% but does not incorporate a mechanism for signal gain.^{52,53} Our approach integrates the contributions of all the pixels along the nonspectral direction of the image, in a similar fashion that the PMT measures all the photons passing through the slit. Finally, the sensor integration time can have an effect on the measurement of incident signal. Both instruments used an integration time of 1 s. On the basis of the above analysis, it is not surprising that the smartphone-based fluorescence spectroscopy is capable of detecting fluorescent output for target molecule concentrations lower than those possible using the particular laboratory instrument used for our comparison. Interestingly, the illumination power available from compact laser sources, combined with the low light sensing capabilities of CMOS cameras within current

(a) Smartphone Fluorimeter



(b) Laboratory Fluorimeter

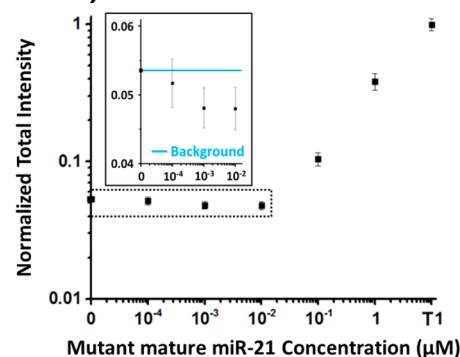


Figure 5. Plots of the normalized total fluorescence intensities as a function of the concentration of mutant mature miR-21. The fluorescence is gathered by (a) a smartphone fluorimeter and (b) a laboratory fluorimeter. The intensity over the wavelength range of 560–580 nm was integrated, and normalized total intensity of the T1 (1 μ M perfectly matched target miR-21) is set to 1 for comparison. Magnified plots that correspond to the dashed area are shown (inset).

smartphones, appears to be compatible with the goal of creating a compact, inexpensive detection instrument for sensing the output of fluorescent assays. While detection of chemical fluorophores represents a heavily used class of labels used for biological assays, the approach demonstrated in this work may also be used for detecting a variety of light emitting materials, including quantum dots, chemiluminescent materials, fluorescent proteins, and phosphorescent dyes.

CONCLUSION

In this work, we demonstrated that the internal camera of a smartphone, combined with a set of optical components for providing wavelength dispersion and a compact, inexpensive green laser pointer, serves the function of a highly sensitive fluorescence spectrometer. By packaging the optical components in the form of a custom cradle that easily interfaces with the smartphone, the system serves as a portable tool for performing fluorescence assays for point-of-use diagnostics applications. We demonstrated operation of the system in the context of a molecular beacon FRET assay for detection of a specific miRNA sequence with 10 pM limits of detection and that the assay was specific against detection of a miRNA sequence that differed from the target sequence by only one base. The demonstrated approach is applicable to any liquid-based assay using a light-emitting reporter, such as fluorescence, quantum dots, chemiluminescence, and phosphorescence. Because the approach measures the spectral output of the assay, it enables separation of light components such as

scattering of the excitation source, donor emission, and acceptor emission. While the laser and sample holder used in the present work were external to the cradle body, a new version of the cradle that is under development will integrate the light source and sample within the cradle body for improved compactness, without loss of functionality. Furthermore, we are presently preparing a smartphone app, which will perform all the computation within the smartphone and direct the user through the steps of calibration, experimental controls, assay steps, and data analysis. In summary, the smartphone-based fluorimeter reported in this work outperforms the laboratory fluorimeter because we utilize a laser light source that more efficiently excites the Cy3 tag than the Xe lamp within the fluorimeter. We do not claim that our system will deliver better sensitivity than *all* fluorimeters, although our results show the mobile system is capable of providing sensitivity that is sufficient for many applications.

■ ASSOCIATED CONTENT

■ Supporting Information

Information about the dimension of the optical cradle. This material is available free of charge via the Internet at <http://pubs.acs.org>.

■ AUTHOR INFORMATION

Corresponding Author

*E-mail: bcunning@illinois.edu.

Notes

The authors declare no competing financial interest.

■ ACKNOWLEDGMENTS

The authors thank Sua Myong and Alex Kreig for providing technical suggestions while performing the Agilent fluorimetry. This work was supported by the National Science Foundation (NSF) under Award No. CBET 1337732.

■ REFERENCES

- (1) Wei, Q.; Qi, H.; Luo, W.; Tseng, D.; Ki, S. J.; Wan, Z.; Göröcs, Z.; Bentolila, L. A.; Wu, T. T.; Sun, R.; Ozcan, A. *ACS Nano* **2013**, *7*, 9147–9155.
- (2) Gallegos, D.; Long, K. D.; Yu, H.; Clark, P. P.; Lin, Y.; George, S.; Natha, P.; Cunningham, B. T. *Lab Chip* **2013**, *13*, 2124–2132.
- (3) Long, K. D.; Yu, H.; Cunningham, B. T. *Biomed. Opt. Express*, submitted.
- (4) Sohn, S. Y.; Bae, W. J.; Kim, J. J.; Yeom, K. H.; Kim, V. N.; Cho, Y. *Nat. Struct. Mol. Biol.* **2007**, *14*, 847–853.
- (5) Bard, F.; Casano, L.; Mallabiabarrena, A.; Wallace, E.; Saito, K.; Kitayama, H.; Guizzunti, G.; Hu, Y.; Wendler, F.; DasGupta, R.; et al. *Nature* **2006**, *439*, 604–607.
- (6) Baughman, J. M.; Perocchi, F.; Girgis, H. S.; Plovanich, M.; Belcher-Timme, C. A.; Sancak, Y.; Bao, X. R.; Strittmatter, L.; Goldberger, O.; Bogorad, R. L.; et al. *Nature* **2011**, *476*, 341–345.
- (7) Baptist, G.; Pinel, C.; Ranquet, C.; Izard, J.; Ropers, D.; Jong, H.; Geiselmann, J. *Nucl. Acids. Res.* **2013**, *41*, No. e164.
- (8) Murphy, M. C.; Ivan, R.; Wei, C.; Timothy, M. L.; Ha, T. *Biophys. J.* **2004**, *86*, 2530–2537.
- (9) Weiss, S. *Nat. Struct. Biol.* **2000**, *7*, 724–729.
- (10) Coto-García, A. M.; Sotelo-González, E.; Fernández-Argüelles, M. T.; Pereiro, R.; Costa-Fernández, J. M.; Sanz-Medel, A. *Anal. Bioanal. Chem.* **2011**, *399*, 29–42.
- (11) Gupta, R.; Kasturi, P.; Bracher, A.; Loew, C.; Zheng, M.; Villella, A.; Garza, D.; Hartl, F. U.; Raychaudhuri, S. *Nat. Methods* **2011**, *8*, 879–884.
- (12) Peterman, E. J. G.; Sosa, H.; Moerner, W. E. *Annu. Rev. Phys. Chem.* **2004**, *55*, 79–96.
- (13) Sun, Y.; Sun, Y.; Stephens, D.; Xie, H.; Phipps, J.; Saroufeem, R.; Southard, J.; Elson, D. S.; Marcu, L. *Opt. Express* **2011**, *19*, 3890–3901.
- (14) Georgakoudi, I.; Jacobson, B. C.; Van Dam, J.; Backman, V.; Wallace, M. B.; Müller, M. G.; Zhang, Q.; Badizadegan, K.; Sun, D.; Thomas, G. A.; Perelman, L. T.; Feld, M. S. *Gastroenterology* **2001**, *120*, 1620–1629.
- (15) Marcu, L. *J. Biomed. Opt.* **2010**, *15*, 011106.
- (16) Borst, J. W.; Visser, A. J. W. G. *Meas. Sci. Technol.* **2010**, *21*, 102002.
- (17) Burchak, O. N.; Mugherli, L.; Ostuni, M.; Lacapère, J. J.; Balakirev, M. Y. *J. Am. Chem. Soc.* **2011**, *133*, 10058–10061.
- (18) Vendrell, M.; Lee, J. S.; Chang, Y. T. *Curr. Opin. Chem. Biol.* **2010**, *14*, 383–389.
- (19) Kepp, O.; Galluzzi, L.; Lipinski, M.; Yuan, J.; Kroemer, G. *Nat. Rev. Drug Discovery* **2011**, *10*, 221–237.
- (20) Deu, E.; Verdoes, M.; Bogoy, M. *Nat. Struct. Mol. Biol.* **2012**, *19*, 9–16.
- (21) Trévisana, M.; Schawaller, M.; Quapil, G.; Souteyrand, E.; Mérieux, Y.; Cloarec, J. P. *Biosens. Bioelectron.* **2010**, *26*, 1631–1637.
- (22) Zuo, X.; Xia, F.; Xiao, Y.; Plaxco, K. W. *J. Am. Chem. Soc.* **2010**, *132*, 1816–1818.
- (23) Liu, F.; Choi, J. Y.; Seo, T. S. *Biosens. Bioelectron.* **2010**, *25*, 2361–2365.
- (24) Freeman, R.; Liu, X.; Willner, I. *J. Am. Chem. Soc.* **2011**, *133*, 11597–11604.
- (25) Zhang, J.; Qi, H.; Li, Y.; Yang, J.; Gao, Q.; Zhang, C. *Anal. Chem.* **2008**, *80*, 2888–2894.
- (26) Cho, M. J.; Lee, U. R.; Kim, Y. S.; Shin, J.; Kim, Y. M.; Park, Y. W.; Ju, B. K.; Jin, J. I.; Choi, D. H. *J. Polym. Sci., Part A: Polym. Chem.* **2010**, *48*, 1913–1918.
- (27) Han, M.; Gao, X.; Su, J. Z.; Nie, S. *Nat. Biotechnol.* **2001**, *19*, 631–635.
- (28) Zhang, C. Y.; Yeh, H. C.; Kuroki, M. T.; Wang, T. H. *Nat. Mater.* **2005**, *4*, 826–831.
- (29) Zhou, D.; Ying, L.; Hong, X.; Hall, E. A.; Abell, C.; Klennerman, D. *Langmuir* **2008**, *24*, 1659–1664.
- (30) Li, M.; Wang, O.; Shi, X.; Hornak, L. A.; Wu, N. *Anal. Chem.* **2011**, *83*, 7061–7065.
- (31) Petryayeva, E.; Algar, W. R. *Anal. Chem.* **2014**, *86*, 3195–3202.
- (32) Baker, M. B.; Bao, G.; Searles, C. D. *Nucleic Acids Res.* **2012**, *40*, No. e13.
- (33) Tan, Y.; Sutanto, E.; Alleyne, A. G.; Cunningham, B. T. *J. Biophotonics* **2014**, *7*, 266–275.
- (34) Bartel, D. P. *Cell* **2004**, *116*, 281–297.
- (35) Bonci, D. *Recent Pat. Cardiovasc. Drug Discovery* **2010**, *5*, 156–161.
- (36) Cheng, Y.; Zhu, P.; Yang, J.; Liu, X.; Dong, S.; Wang, X.; Chun, B.; Zhuang, J.; Zhang, C. *Cardiovasc. Res.* **2010**, *87*, 431–439.
- (37) Haider, K. H.; Idris, N. M.; Kim, H. W.; Ahmed, R. P.; Shujia, J.; Ashraf, M. *Cardiovasc. Res.* **2010**, *88*, 168–178.
- (38) Cheng, Y.; Liu, X.; Zhang, S.; Lin, Y.; Yang, J.; Zhang, C. *J. Mol. Cell. Cardiol.* **2009**, *47*, 5–14.
- (39) Morrissey, E. E. *J. Clin. Invest.* **2010**, *120*, 3817–3819.
- (40) Cheng, Y.; Zhang, C. *J. Cardiovasc. Transl. Res.* **2010**, *3*, 251–255.
- (41) Dong, S.; Cheng, Y.; Yang, J.; Li, J.; Liu, X.; Wang, X.; Wang, D.; Krall, T. J.; Delphin, E. S.; Zhang, C. *J. Biol. Chem.* **2009**, *284*, 29514–29525.
- (42) Frezzetti, D.; Menna, M. D.; Zoppoli, P.; Guerra, C.; Ferraro, A.; Bello, A. M.; Luca, P. D.; Calabrese, C.; Fusco, A.; Ceccarelli, M.; et al. *Oncogene* **2011**, *30*, 275–286.
- (43) Ma, X.; Kumar, M.; Choudhury, S. N.; Buscaglia, L. E. B.; Barker, J. R.; Kanakamedala, K.; Liu, M. F.; Li, Y. *Proc. Natl. Acad. Sci. U.S.A.* **2011**, *108*, 10144–10149.
- (44) Tyagi, S.; Kramer, F. R. *Nat. Biotechnol.* **1996**, *14*, 303–308.
- (45) Ke, G.; Wang, C.; Ge, Y.; Zheng, N.; Zhu, Z.; Yang, C. *J. Am. Chem. Soc.* **2012**, *134*, 18908–18911.

- (46) Kim, J. H.; Chaudhary, S.; Ozkan, M. *Nanotechnology* **2007**, *18*, 195105.
- (47) Li, J. J.; Chu, Y.; Lee, B. Y.; Xie, X. S. *Nucleic Acids Res.* **2008**, *36*, No. e36.
- (48) Seth, D.; Chakrabarty, D.; Chakraborty, A.; Sarkar, N. *Chem. Phys. Lett.* **2005**, *401*, 546–552.
- (49) Wu, P.; Brand, L. *Anal. Biochem.* **1994**, *218*, 1–13.
- (50) Smith, A. R. *Comput. Graphics* **1978**, *12*, 12–19.
- (51) Mortensen, K. I.; Churchman, L. S.; Spudich, J. A.; Flyvbjerg, H. *Nat. Methods* **2010**, *7*, 377–381.
- (52) Rhodes, H.; Tai, D.; Qian, Y.; Mao, D.; Venezia, V.; Zheng, W.; Xiong, Z.; Liu, C. Y.; Ku, K. C.; Manabe, A.; et al. The Mass Production of BSI CMOS Image Sensors. In *Proceedings of the 2009 International Image Sensor Workshop*, Bergen, Norway, June 22–28, 2009; pp 27–32.
- (53) Meynants, G.; Bogaerts, J.; Wang, X.; Vanhorebeek, G. Backside Illuminated Global Shutter CMOS Image Sensors. In *Proceedings of the 2011 International Image Sensor Workshop*, Hokkaido, Japan, June 8–11, 2011; pp 305–309.